

Conformational Changes of a Calix[8]arene Derivative at the Air–Water Interface

Gustavo de Miguel,[†] José M. Pedrosa,[‡] María T. Martín-Romero,^{*,†} Eulogia Muñoz,[†] Tim H. Richardson,[§] and Luis Camacho^{*,†}

Departamento de Química Física y Termodinámica Aplicada, Universidad de Córdoba, Campus Universitario de Rabanales, Ed. Marie Curie, E-14071 Córdoba, Spain, Departamento de Ciencias Ambientales, Universidad Pablo de Olavide, Crta. Utrera km 1, E-41013 Sevilla, Spain, and Physics and Astronomy Department, University of Sheffield, Hicks Building, Hounsfield Road, Sheffield S3 7RH, United Kingdom

Received: September 14, 2004

The particular behavior of a *p*-tert-butyl calix[8]arene derivative (C8A) has been studied at the air–water interface using surface pressure–area isotherms, surface potential–area isotherms, film relaxation measurements, Brewster angle microscopy (BAM), and infrared spectroscopy for Langmuir–Blodgett films. Thus, it is observed that the properties of the film, for example, isotherms, domain formation, and FTIR spectra, recorded during the first compression cycle differ appreciably from those during the second compression and following cycles. The results obtained are interpreted on the basis of the conformational changes of the C8A molecules by surface pressure, allowing us to inquire into the inter- and intramolecular interactions (hydrogen bonds) of those molecules. Thus, the compression induces changes in the kind of hydrogen bonds from intra- and intermolecular with other C8A molecules to hydrogen bonds with water molecules.

Introduction

Over the past three decades, calixarene chemistry has been established as a readily available molecular platform on which to build a wide variety of interesting cavity-containing and multifunctional molecules. The great interest in calixarenes is based on their broad potential in designing supramolecular host–guest structures and their close relation to current topics such as selective molecular recognition of biorelevant species, metal cation complexation, design and synthesis of enzyme-mimic systems, or gas sensing.^{1,2} However, as considered for other potential systems, it is important to have a material with a well-controlled organization and thickness. In that sense, a better understanding and control of the molecular orientational and conformational changes of these systems is obviously needed to obtain a methodology for engineering different functional surfaces.

During the past decade, some interesting work on the behavior of different calixarenes at the air–water interface has been published. Calix[6]arenes in monolayers at the air–water interface were studied to establish stability, physicochemical properties, and conformations at the interface. A reorientation of the calixarene in this system from cone parallel to perpendicular with respect to the interface was observed under compression.³ Also, a study of the behavior of calix[8]arene monolayers as a function of temperature and spreading solvent for understanding the calixarene conformation at the air–water interface can be found.⁴

Some calixarenes with short or without any alkyl chains have been found to form monolayers at the air–water interface. Particularly, Langmuir monolayers of *p*-tert-butylcalixarene have been studied. For example, Richardson and Stirling prepared

monolayers of *p*-tert-octylcalix[8]arenes with lower rims substituted with carboxylic, ketone, and amino groups.^{5–7}

Many derivatives of calix[*n*]arenes with *n* = 4, 6, and 8 have been synthesized and with different hydrophilic groups and alkyl chains, and although the structure of those derivatives is different, it is noteworthy, for example, that the isotherms frequently are not reproducible and depend on the organic spreading solvent,^{3,4,8} compression speed,⁹ and spreading concentration, that is, on every mechanical and thermal process during the preparation of the monolayer. Therefore, it is possible to observe the coexistence between solid irregular domains and the gas phase at low surface pressure.⁹

However, some similarities in the interfacial behavior of *p*-tert-butyl-calix[*n*]arenes have been detected. In the surface pressure–area isotherms (π –*A* isotherms), a flat plateau without inclination at areas lower than those expected for maximum packing of the molecules could be appreciated. This observation has been related to a transition from a tightly packed monolayer to a bilayer/multilayer structure.^{6,10–12} However, when those calixarenes are functionalized with small hydrophilic groups, such as OH groups, a dimer formation with perpendicular orientation with respect to the interface has been proposed.^{3,11}

In this work, a *p*-tert-butyl calix[8]arene derivative (C8A) is studied at the air–water interface. The C8A forms stable Langmuir films at the air–water interface, demonstrating its amphiphilic character. The calixarene behavior in the films has been studied using surface pressure–area isotherms, surface potential–area isotherms, film relaxation measurements, Brewster angle microscopy (BAM), and infrared spectroscopy for Langmuir–Blodgett films. The results obtained are interpreted on the basis of the conformational changes of the C8A molecules by surface pressure, allowing us to inquire into the inter- and intramolecular interactions (hydrogen bonds) of those molecules. Thus, we observed that the compression induces changes in the kind of hydrogen bonds from intra- and intermolecular with other C8A molecules to hydrogen bonds with water molecules.

* To whom correspondence should be addressed. E-mail: qf1marot@uco.es.

[†] Universidad de Córdoba.

[‡] Universidad Pablo de Olavide.

[§] University of Sheffield.

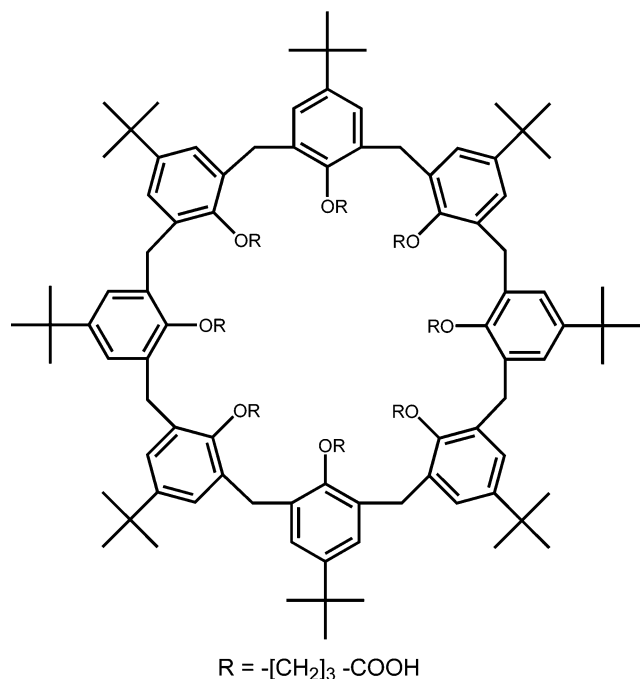


Figure 1. Chemical structure of carboxylic-acid-substituted calix[8]-arene.

This phenomenon has repercussions in the conformation of the calixarene rim, that is, on the shape and accessibility of the central cavity of C8A, and it can be used to extend the possible applications of these types of molecules alongside using other strategies such as modification of substituents both on the upper and lower rim or the number of repeat units in the calixarene.

Experimental Section

Materials. The calixarene compound, C8A, whose general structure is shown in Figure 1, was synthesized at Sheffield University by Davis et al. and used without further purification.^{14,15}

Pure chloroform as spreading solvent was obtained from Merck and used as received. Ultrapure water from a Milli-Q-Plus system was used throughout.

Methods. Monolayers of the C8A were prepared on pure water at pH 5.7 and 21 °C. After evaporation of the organic solvent, the monolayer was compressed or expanded using a movable barrier on a Nima rectangular trough provided with a filter paper Wilhelmy plate¹⁶ with a compression velocity of $10\text{--}20 \text{ \AA}^2 \text{ molecule}^{-1} \text{ min}^{-1}$, facilitating the recording of surface pressure–area (π – A) isotherms. The system was also equipped with a vibrating capacitor device, Kelvin Probe SP1 (Nanofilm, Germany), for measurement of the surface potential–area (ΔV – A).

Brewster angle microscopy (BAM) was used to gain additional information on the molecular organization of C8A in monolayers at the air–water interface. Images of the film have been recorded with a lateral resolution of $2 \text{ }\mu\text{m}$ (I-Elli2000 supplied by NFT, Nanofilm Technologie, Göttingen, Germany). The image-processing procedure included a geometrical correction of the image as well as a filtering operation to reduce interference fringes and noise. Furthermore, the brightness of each image was scaled to improve contrast. The size of the images is $430 \text{ }\mu\text{m}$ in width. The microscope and film balance were located on a table with vibration isolation (antivibration system MOD-2 S, Halcyonics, Göttingen, Germany) in a large class 100 clean room.

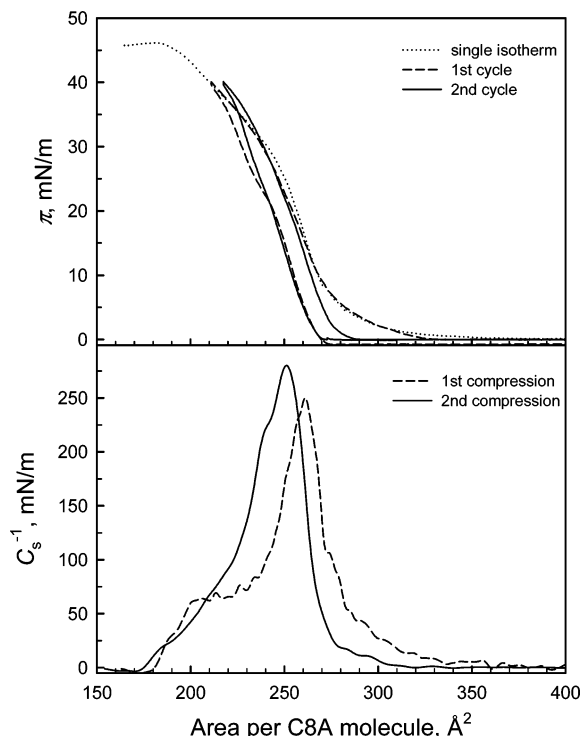


Figure 2. (Top) π – A single isotherm of C8A (dotted line) and compression–expansion cycles: first cycle (dashed line) and second cycle (solid line). (Bottom) Compressibility moduli (C_s^{-1}) versus area (A) for the C8A monolayers at the air–water interface under compression processes from first and second cycles, solid and dashed lines, respectively.

The C8A multilayers were assembled by sequential monolayer transfer, that is, withdrawal (\uparrow) and immersion (\downarrow) of the substrate through the interface covered with the calixarene film. The transfer ratio, τ , was dependent on the surface pressure selected for the transfer process. The different values of τ will be indicated along the corresponding section. The monolayers were transferred onto a CaF_2 substrate which was cleaned several times with CHCl_3 and rinsed with pure water.

FTIR measurements were performed on a Mattson Research Series instrument equipped with a DTGS detector. The background spectrum of an uncoated CaF_2 substrate was recorded as the reference. The FTIR transmission spectra of the films were measured with and without polarized light (s and p) under different incidence angles.

The molecular mechanics simulations of the Calix(8) were carried out using the HyperChem molecular modeling package (version 6).¹⁷ The geometry of the molecule was preoptimized using the Amber96 force field with no partial charges. Then, the charges were assigned using the AM1 semiempirical method. Next, the geometry was again optimized using Amber. The procedure was repeated until convergence was achieved (the convergence criteria for geometrical optimization was $0.001 \text{ kcal}/(\text{\AA}\cdot\text{mol})$). A similar method of assigning partial charges was used recently for other calixarene derivatives.^{11,18} After charges were assigned, three runs of the molecular dynamics simulations were performed to search for the possible existence of other structures with lower energy. Each run consisted of heating the structure to 300 K, molecular dynamics simulations for 5 ps, and then annealing to 0 K.

Results

Surface Pressure–Area Isotherms. The surface pressure–area (π – A) isotherm of the C8A is shown in Figure 2 (top,

dotted line). Several measurements were registered, and as observed in Figure 2 (dotted line), the surface pressure starts rising at an area of $A_0 \approx 320 \text{ \AA}^2/\text{molecule}$ (the deviation found for more than five experiments was $\sim 10\%$), in good agreement with results published elsewhere.¹⁹ Under further compression, a continuous rise of the isotherm resembling those presented by condensed phase is detected, although there is no sharply definable start of the one-phase region. This behavior is different from that of typical amphiphilic monolayers, suggesting a phase transition between the gas phase and a condensed phase. Also, during the continuous rise of the isotherm, several smooth changes in the slope of the π - A isotherm can be seen. Finally, further compression of the C8A film up to high surface pressures causes a different collapse from that shown by typical amphiphilic monolayers, that is, strong reduction of the surface pressure. When the film reaches $\sim 200 \text{ \AA}^2/\text{molecule}$ ($\pi = 46 \text{ mN/m}$), the surface pressure decreases slightly and a long plateau region up to $\sim 90 \text{ \AA}^2/\text{molecule}$, where the surface pressure slightly increases again, could be seen.

To study the homogeneity of the film, successive compression-expansion cycles were recorded for the C8A film. As an example, first and second cycles are shown in Figure 2 (top, dashed and solid lines for the first and second cycles, respectively). In the low-surface-pressure region, the surface area during the first cycle is larger with respect to the second compression, although the isotherms recorded during the expansion processes are totally coincident below 25 mN/m , showing a slight hysteresis with respect to the compression. However, a notorious phenomenon can be appreciated during the compression processes in the high-surface-pressure region, where a crossing between both isotherms producing an expansion of $\sim 10 \text{ \AA}^2$ for the second cycle with respect to the first is detected. Further compression-expansion cycles showed identical isotherms to those recorded for the second cycle. The crossing phenomenon described during the two first successive compression cycles was observed for all experiments thus performed (at least five experiments) and was independent of spread area.

Because of the singular behavior of these isotherms, that is, there are no sharp phase transitions, determination of the area per molecule is difficult. During the continuous rise of the isotherm, several smooth changes of the π - A isotherm slope are observed. Thus, the slope decreases at ~ 260 and $250 \text{ \AA}^2/\text{molecule}$ for the first and second compression processes, respectively.

A possible approach is the assignment of a maximum packing to the area at which the maximum slope of the π - A isotherm is found, that is, the area at which the compressibility modulus is maximum. The compressibility modulus, C_s^{-1} , of a lipid monolayer is defined as

$$C_s^{-1} = -A \left(\frac{\partial \pi}{\partial A} \right)_T \quad (1)$$

Figure 2 (bottom) plots the compressibility modulus versus the surface area measured during two successive compression cycles up to $\sim 180 \text{ \AA}^2/\text{molecule}$, according to eq 1. Thus, the maximum values of the compressibility modulus, $(C_s^{-1})_{\text{max}}$, for those compression processes were $(C_s^{-1})_{\text{max}} = 250 \pm 10 \text{ mN m}^{-1}$ ($A = 261 \text{ \AA}^2$ and $\pi = 16 \text{ mN m}^{-1}$) and $(C_s^{-1})_{\text{max}} = 280 \pm 10 \text{ mN m}^{-1}$ ($A = 250 \text{ \AA}^2$ and $\pi = 22 \text{ mN m}^{-1}$), respectively. Henceforth, the isotherm slopes decrease, which is indicative of a loss of the rigidity within the monolayer. This fact suggests that the solid phase is not achieved. Anyway, the films seem to be very flexible, as deduced from the high values of the

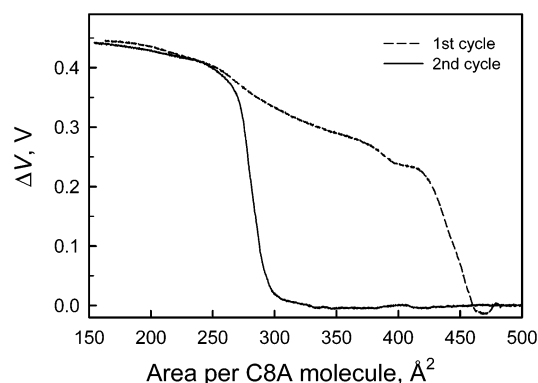


Figure 3. ΔV - A isotherms of C8A during the first compression (dashed line) and second compression (solid line) processes.

compressibility modulus. According to the literature,²⁰ the compressibility modulus values range from 12.5 to 50 mN m^{-1} for liquid-expanded films, while for a liquid-condensed phase it varies from 100 to 250 mN m^{-1} . The maximum values of C_s^{-1} for each case corresponding to the closest packing of the monolayer evidence the state of the C8A monolayer as liquid-condensed phase at the air-water interface.

Surface Potential-Area Isotherms. Simultaneously to the π - A isotherm, the surface potential-area isotherms were recorded to obtain supporting information concerning the behavior of the C8A film during the two successive compression processes at the air-water interface. Figure 3 shows the ΔV - A isotherms recorded during the first and second compression processes (dashed and solid lines, respectively). Clearly, a different shape is observed for each isotherm. During the first compression cycle, the surface potential starts increasing at $A \approx 460 \text{ \AA}^2/\text{molecule}$, while for the second cycle it occurs at $A \approx 300 \text{ \AA}^2/\text{molecule}$. The surface potential converges to a maximum value at $A < 250 \text{ \AA}^2/\text{molecule}$ in both cases. The behavior of the film during the second cycle is very interesting: the potential value remains zero from 500 to $300 \text{ \AA}^2/\text{molecule}$. According to the area per C8A in the flat orientation, at $\sim 320 \text{ \AA}^2$ (corresponding to the A_0 value measured in the isotherms, Figure 2 (top, dotted line)) a whole monolayer is expected and therefore the buildup in the surface potential should occur in the 480 - 320 \AA^2 region, as recorded for the first cycle.

Brewster Angle Microscopy. The C8A monolayer formed at the air-water interface was directly observed by BAM. Figure 4 shows the morphology and behavior of that film during the two successive compression-expansion cycles. Some images at different surface area (indicated at the bottom of each photo) taken during the first compression (1st c), successive first expansion (1st e), following second compression (2nd c), and expansion (2nd e) are shown as examples.

The images show clear differences between both cycles, which correlate with the results recorded during the surface pressure-area and surface potential-area isotherms. At low surface pressure (immediately after spreading), the film presents a two-phase-coexistence region showing large irregular solid domains (bright regions) and channels of gas phase (dark regions) (image i) are easily recognized. As the film is compressed, the solid domains do not coalesce easily but tend to collide with each other, producing channels of gas phase (image ii). Under further compression, the gas phase becomes extinct and the bright region covers the whole field of view (images iii and iv). No expanded-liquid phases were observed as suggested by Castillo et al.⁹ when describing a similar phenomenon with a different calixarene derivative.

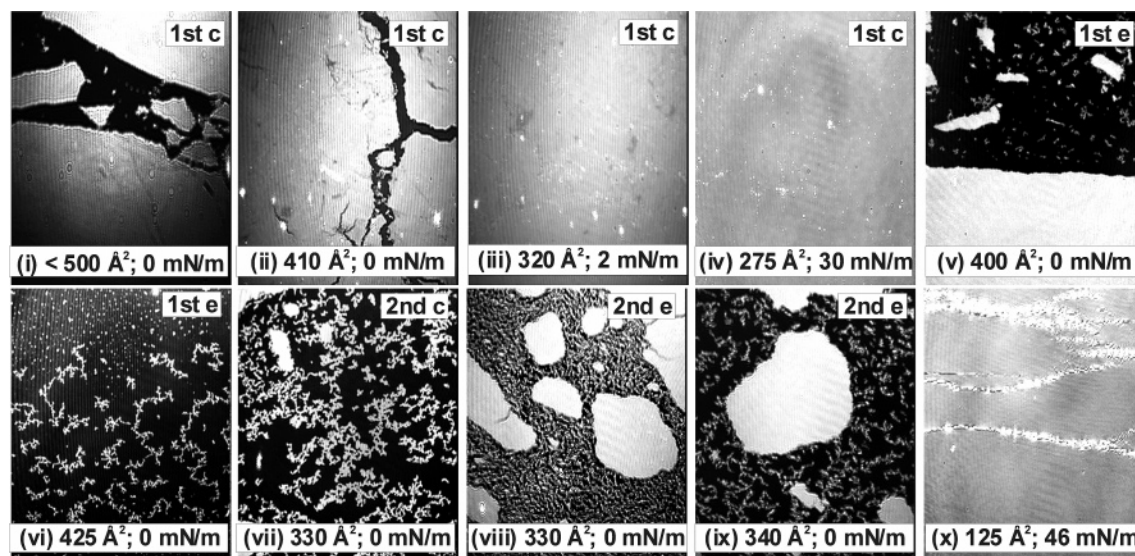


Figure 4. Brewster angle microscope (BAM) images of C8A monolayer at the air–water interface during the two successive cycles: first compression (1st c), first expansion (1st e), second compression (2nd c), second expansion (2nd e), processes and collapse of the film, images i–iv, images v–vi, image vii, images viii–ix, and image x, respectively.

During the first expansion process, a peculiar morphology is observed: as the film was expanded, the large bright domains break apart, producing new small branchlike domains (images v and vi) which were not previously observed during the first compression process. During the subsequent compression process, the morphologies at both low and high surface pressures are similar to those observed during the expansion of the first cycle, that is, small branchlike domains are observed (image vii). Furthermore, a consecutive second expansion process produces a similar effect to that observed during the first expansion and second compression processes (images viii and ix).

Further compression of the C8A monolayer up to $A < 150$ Å²/molecule induced bright striations in the film, probably because of the collapse of the monolayer (image x). Surprisingly, above 40 mN/m ($A < 200$ Å²/molecule) no morphological changes were observed in the region of focus, although a reduction in the molecular area was measured. Also, the ellipsometric data (not shown) suggested no thickness changes for this region and that observed at $A \approx 300$ Å²/molecule. The reduction of the surface area measured would imply a reorganization of the monolayer. The striations (image x) were effectively found out of the focus region, very close to the movable barriers, and acted as nucleation centers for multilayer formation.

Castillo et al.,⁹ for a calix[8]arene derivative, observed that at low surface pressure just before the image was recorded the bright domains suddenly broke apart. That phenomenon was attributed to a tiny vibration produced on the surface, as a result of moving the objective of the microscope when focusing the area under study. We also observed a similar effect with the vanishing of the domains, although the film returned into view when the shutter of laser was switched. Therefore, it seems that the above phenomenon is due to the tiny vibration by the laser on the film. In this system, there is not only a segregation of domains, but also an increasing of the kinetic energy, leading to the melting of the former phase.

Furthermore, this effect was less noticeable during the first compression process than during the second consecutive one. Maybe domains formed by strong intermolecular forces (large irregular bright domains) are little affected by the vibration. However, after the first compression–expansion cycle, domains

with weaker intermolecular interactions (branchlike domains) can more easily absorb that small amount of energy (arising from the vibration), leading to segregation and vanishing of the domain from the focused region.

This phenomenon may be also produced by means of the device used in this work for measuring surface potential. In the vibration–plate method, the air electrode is moved closer to the water surface, thus yielding a tiny vibration and being able to transfer enough energy for segregation of small domains (or domains with weaker intermolecular interactions). It could explain the absence of surface-potential signal ($\Delta V = 0$ from 500 to 300 Å²/molecule) during the second compression cycle.

The morphology of the C8A monolayer during the two successive compression–expansion cycles leads us to consider a change in the conformation of the calixarene molecules under compression to explain the crossing observed between the two isotherm cycles (see Figure 2). However, such a change would not imply a reorientation, that is, from a parallel to perpendicular, at least for surface pressures below 40 mN/m (see Figure 2, top), since it should produce a much greater reduction of the surface area.

The conformational change caused as a result of the compression produces small changes on both the compressibility and the packing of the C8A units. However, the effect on the morphology and stability of the domains seems to occur owing to the differences between the intermolecular interactions occurring within the two successive compression–expansion cycles.

To infer the conformational change, the films fabricated at the air–water interface during the two successive compression processes were transferred onto CaF₂ and a detailed study using infrared spectroscopy was carried out.

FTIR Spectroscopy of C8A Multilayers. Monolayers of C8A at different surface pressures were transferred to CaF₂ substrates by the Langmuir–Blodgett (LB) method. Y-type LB films were obtained, the average transfer ratio being $\tau \approx 0.7$ at 25 mN/m and $\tau \approx 0.9$ at 35 mN/m. The different transferred LB films were studied by FTIR. In Figure 5, the FTIR spectra corresponding to the LB films transferred at 35 mN/m (A) during the first (dotted line) and second (solid line) successive compression processes and at 25 mN/m (B) are shown. Also, a cast film on CaF₂ (C) is shown for comparison.

TABLE 1: Band Positions and Assignments for FTIR Transmission Spectra of LB Films Containing 21 Monolayers of C8A Transferred at 35 mN/m

band position, cm ⁻¹	assignment	band position, cm ⁻¹	assignment	band position cm ⁻¹	assignment
2959	$\nu_{\text{as}}(\text{CH}_3)$	1480	benzene ν_{19}	1243	$\nu(\text{C}-\text{O}-\text{C})$, =CO stretch (ether)
2920	$\nu_{\text{as}}(\text{CH}_2)$	1460	$\delta(\text{CH}_2)$	1204	CH benzene bend
2869	$\nu_{\text{s}}(\text{CH}_3)$	1445	benzene ν_{19}	1186	CH benzene bend
2851	$\nu_{\text{as}}(\text{CH}_2)$	1413	$\delta(\text{CH}_2)$, attached to CO	1111	CH benzene bend
1738	$\nu(\text{C}=\text{O})$ free	1390	$\delta(\text{CH}_3)$, umbrella mode	1084	CO stretching (ether) =C-O-C (1120–1020)
1708	$\nu(\text{C}=\text{O})$ H-bond	1383	$\delta(\text{CH}_3)$ deform tert-butyl	1043	CH benzene bend
1584	benzene ν_8	1362	deform tert-butyl or $\nu(\text{benzene ring})$		
1548	$\nu_{\text{as}}(\text{COO}^-)$	1288	benzene ν_{14}		

The typical characteristic frequencies assigned to the alkyl chains, aromatic rings, and carbonyl groups can be noted in those spectra. In Table 1, the band positions and their assignments^{8,21–30} for FTIR transmission spectra of LB films containing 21 monolayers of C8A transferred at 35 mN/m are given. However, this assignment is not totally complete since we were not able to assign different stretching modes involved in some registered bands.

The band positions are recognized for all spectra. However, a meaningful difference between those spectra from LB films transferred at 25 and 35 mN/m can be appreciated; thus, the peaks at ~ 2920 and 2850 cm⁻¹ associated with symmetric and antisymmetric stretching vibrations of the CH₂ groups are more pronounced for the film transferred at 35 mN/m. Also, those differences are observed between the LB film at 35 mN/m and the cast film.

Furthermore, when we compare the FTIR spectra obtained from the LB films transferred during the first and second successive compression processes, significant differences within the high-frequency region, that is, 3000–2800 cm⁻¹, were observed for those at 35 mN/m (Figure 5A: dotted and solid lines, for first and second compressions, respectively). In contrast, almost no differences were found for those at 25 mN/m from the two compression processes (data not shown).

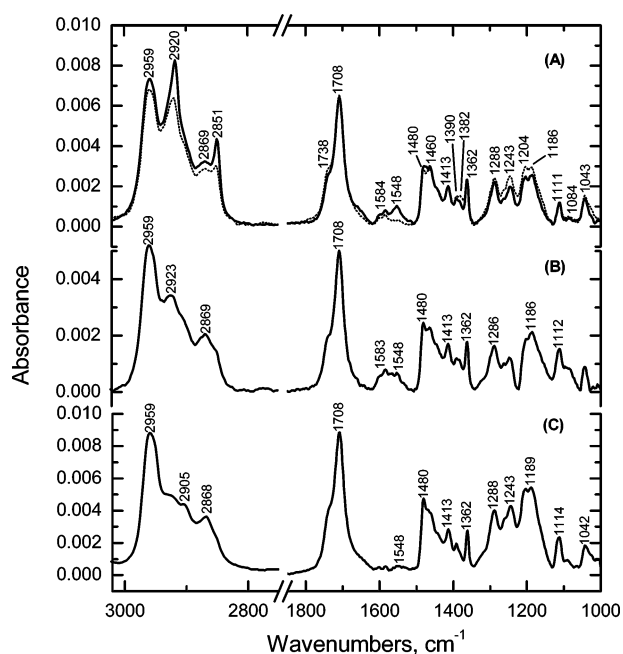


Figure 5. FTIR transmission spectra of 21 layers of C8A transferred on both sides of the CaF₂ substrates at 35 mN/m (A) (dotted and solid lines, for first and second compressions, respectively) and 25 mN/m (B). As a reference, the spectrum of C8A film by casting on CaF₂ is also shown (C).

Also, the relative intensities of the peaks at 2917 and 2849 cm⁻¹ increase regarding the other peaks for the spectrum corresponding to the second cycle (Figure 5A, solid line). Moreover, the peak at 1548 cm⁻¹ increases.

Next, the high wavenumber region (3000–2800 cm⁻¹) and the region of the C=O stretching mode will be analyzed in detail.

CH Stretching Region (3000–2800 cm⁻¹). In Figure 6, the FTIR spectra obtained from the LB and cast films (35 mN/m, first compression, dotted line; 35 mN/m, second compression, solid line; 25 mN/m, dashed line; and cast film, dash-dotted line) in the high wavenumber region are shown for better comparison. The original spectra (from Figure 5) have been normalized with respect to the $\nu_{\text{as}}(\text{CH}_3)$ mode.

Previous IR studies^{21–26,31–39} have shown that the location of $\nu_{\text{s}}(\text{CH}_2)$ and $\nu_{\text{as}}(\text{CH}_2)$ modes are sensitive indicators of both the orientation and the lateral interactions between alkyl chains. To analyze the differences between the vibration modes in this spectral region, the experimental data (data from Figure 6) were fitted to Gaussian functions. Figure 7 shows the normalized data (solid line) and the calculated Gaussian functions (dotted line) for the cast film (A), LB films transferred at 25 and 35 mN/m during the first cycle (B and C, respectively), and at 35 mN/m during the second successive compression process (D).

In the cast film (A), four Gaussian functions were needed to obtain a good fit of the experimental data with the following maxima: 2928 cm⁻¹ associated with the stretching mode of $\nu_{\text{as}}(\text{CH}_2)$ and 2958 cm⁻¹ assigned to the $\nu_{\text{as}}(\text{CH}_3)$ mode and^{22,29,40–43} 2870 and 2902 cm⁻¹ that will be assigned in Table 2.

However, five Gaussian functions were needed to fit successfully the FTIR spectra of the LB film transferred at 25 mN/m (B). In comparison with the fitting of the cast film, two

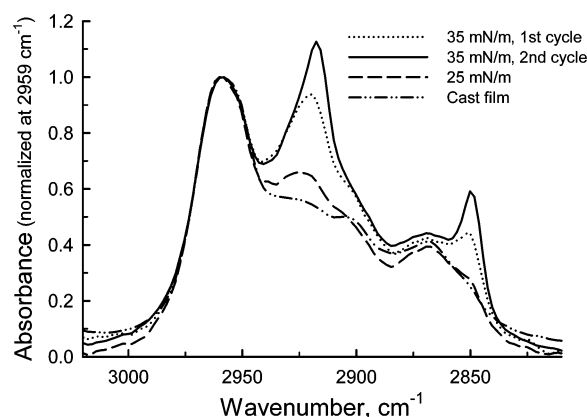


Figure 6. FTIR transmission spectra of 21 layers of C8A transferred on both sides of the CaF₂ substrates at 35 mN/m during the first (dashed line) and second (solid line) compression cycles.

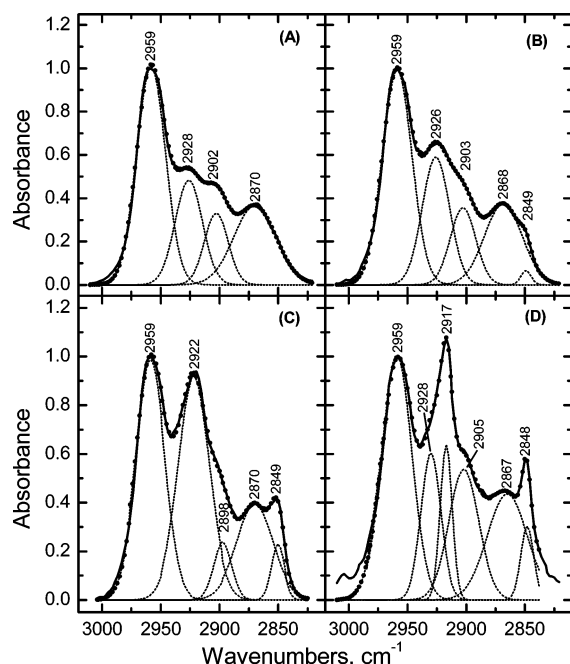


Figure 7. FTIR spectra from experimental data (solid line) and the calculated Gaussian functions (dotted line) for (A) cast films, (B) LB films transferred at 25 mN/m during the first cycle, (C) LB films transferred at 35 mN/m during the first cycle, and (D) LB films transferred at 35 mN/m during the second. The experimental data have been normalized with respect to the $\nu_{\text{as}}(\text{CH}_3)$ mode.

TABLE 2: Band Positions, Assignments, Wavelength Half-Width (fwhm), and Dichroic Ratio at 60° Incidence of the Gaussian Functions Corresponding to the FTIR Spectrum of the Film Transferred to 35 mN/m during the Second Compression Cycle

ν , cm^{-1}	assignment	fwhm, cm^{-1}	A_s/A_p , $i = 60^\circ$
2959	$\nu_{\text{as}}(\text{CH}_3)$	32	1.40
2928	$\nu_{\text{as}}(\text{CH}_2)_{\text{liq}}$	20	1.44
2917	$\nu_{\text{as}}(\text{CH}_2)_{\text{cry}}$	11	2.46
2905 ^a	$\nu_{\text{s}}(\text{CH}_2)_{\text{FR}} + \nu_{\text{s}}(\text{CH}_3)$	30	1.63
2867 ^b	$\nu_{\text{s}}(\text{CH}_3)_{\text{FR}} + \nu_{\text{s}}(\text{CH}_2)_{\text{liq}}$	43	1.82
2848	$\nu_{\text{s}}(\text{CH}_2)_{\text{cry}}$	9	2.48

^a May be assigned to a combination of the $\nu_{\text{s}}(\text{CH}_3)$ mode and $\nu_{\text{s}}(\text{CH}_2)_{\text{FR}}$ mode that can emerge within the 2895–2907 cm^{-1} region.⁴⁴ ^b May be assigned to the $\nu_{\text{s}}(\text{CH}_3)_{\text{FR}}$ mode vibrating in the 2875–2880 cm^{-1} region⁴⁵ and $\nu_{\text{s}}(\text{CH}_2)_{\text{liq}}$ (at 2856 cm^{-1}). FR, Fermi Resonance.

differences can be identified: (1) the relative increase of the CH_2 modes and (2) the emergence of a new small peak at 2849 cm^{-1} .

Also, a minimum of five Gaussian functions for a good fit was needed for the spectrum of the LB film transferred at 35 mN/m (C) during the first compression process. The peaks corresponding to 2849, 2870, and 2959 cm^{-1} emerge approximately at the same wavenumbers as in the previous cases, although the peak at 2928 cm^{-1} shifts to 2922 cm^{-1} and increases its fwhm (full width at half-maximum) and that at 2902 cm^{-1} goes to 2898 cm^{-1} , decreasing its fwhm. These shifts must be interpreted as a poor resolution of bands in the corresponding wavenumber region, probably because of an overlapping with a new peak.

On the other hand, at least six Gaussian functions are needed to fit the FTIR spectrum of the film transferred at 35 mN/m during the second successive compression process. The corresponding band positions, assignments, and fwhm are shown in Table 2.

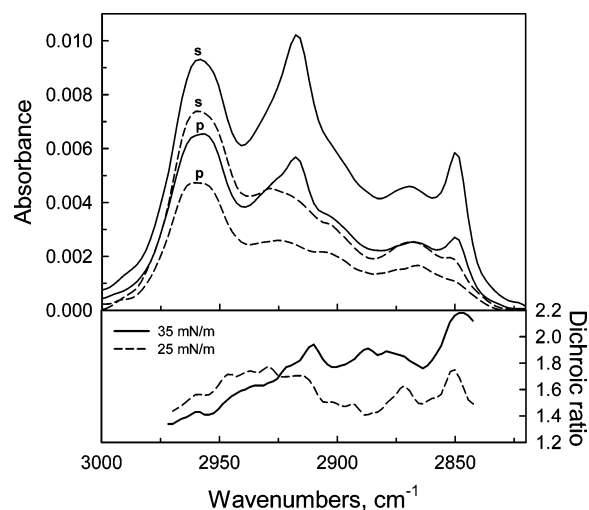


Figure 8. (Top) Polarized IR spectra, s and p, under 60° incidence of LB films transferred on CaF_2 : solid line, 35 mN/m during the second compression cycle; dashed line, 25 mN/m during the first compression cycle. (Bottom) Plot of the dichroic ratios versus wavelength.

By analyzing the data shown in Figure 7 and Table 2, two phenomena stand out: (1) the peak corresponding to the $\nu_{\text{as}}(\text{CH}_3)$ stretches remains practically unchanged for all studied films and (2) the difference found in the spectra should be related to the stretching vibrations of the CH_2 group.

As well described in the references,^{21–25,31–39} the band positions of the $\nu(\text{CH}_2)$ modes (antisymmetric and symmetric) can reveal the structural state of the alkyl chains. Therefore, the values being equal to or smaller than 2920 and 2850 cm^{-1} for $\nu_{\text{as}}(\text{CH}_2)$ and $\nu_{\text{s}}(\text{CH}_2)$ modes, respectively, should correspond to a crystalline state, while band positions at 2928 and 2856 cm^{-1} for those vibrating modes, respectively, should be proceed from a liquid state (noted allocation in Table 2). Likewise, the fwhm of the $\nu_{\text{as}}(\text{CH}_2)$ mode has been used to provide the adlayer order.^{21,37,46,47} Thus, a bandwidth narrower than 20 cm^{-1} has been related to a crystalline state, while a broader peak would correspond to a disordered liquid state. Consequently, the peaks obtained for the film transferred at 35 mN/m during the second cycle at 2917 ($\nu_{\text{as}}(\text{CH}_2)$) and 2848 cm^{-1} ($\nu_{\text{s}}(\text{CH}_2)$) and, also taking into account their fwhm values, should be related to a highly ordered structure of the alkyl chains.

To estimate the average tilt of different groups with respect to the normal surface, transmission spectra under polarized light, s and p, and at different incidence angles were measured. Figure 8 (top) shows the polarized spectra in the 3000–2800 cm^{-1} wavenumber region for LB films transferred at 35 (second cycle, solid line) and 25 mN/m (first cycle, dashed line) under 60° incidence. The results have been interpreted by using the dichroic ratio $D = A_s/A_p$ (Figure 8, bottom).

For very thin films and following the treatment developed by Vandevyver et al.⁴⁸ it is possible to write

$$D = \frac{A_s}{A_p} \approx \left(\frac{n_1 \cos(r) + n_3 \cos(i)}{n_1 \cos(i) + n_3 \cos(r)} \right) \times \left(\frac{2n_1^3 n_3 \sin(i)^2 \langle \cos(\theta)^2 \rangle}{n_2^4 \langle \sin(\theta)^2 \rangle + \cos(i) \cos(r)} \right)^{-1} \quad (2)$$

where n_1 (=1), n_2 , and n_3 (=1.41) are the refractive index of air, film, and CaF_2 , respectively; $r = \arcsin((n_1 \sin(i)/n_3))$ is obtained from the Snell ratio, i and θ are angles of the incidence and the transition dipole, respectively, and brackets denote

average values. According to eq 2 and with $i = 60^\circ$ and $\theta = 90^\circ$ (perpendicular orientation) and considering $n_2 = 1.45$, $D = 2.35$ was calculated, while with $i = 60^\circ$ and $\theta = 54.7^\circ$ (random orientation), eq 2 predicts $D = 1.46$.

For the film transferred at 35 mN/m (Figure 8, bottom, solid line), D ranges between 1.4 and 2.2 at 2958 and 2850 cm^{-1} , respectively, which indicates a random orientation for the $-\text{CH}_3$ (tert-butyl) groups and an orientation close to perpendicular for the stretch $\nu_s(\text{CH}_2)_{\text{cry}}$ mode. In as much as the vibration of that stretching $\nu_s(\text{CH}_2)_{\text{cry}}$ mode is in the plane of H-C-H atoms, the alkyl chain should be close to normal with respect to the support. However, in the film transferred to 25 mN/m (Figure 8, bottom, dashed line), D obtained is more complex to interpret since in the wavenumber regions dominated by the CH_2 stretching modes D values ($D \approx 1.7\text{--}1.8$) are larger than those obtained ($D \approx 1.4\text{--}1.5$) in the region of the stretching CH_3 mode.

We have tried to determine the D values for each of the Gaussian peaks previously fitted (data from Figure 7). However, this procedure was not feasible for both the cast and the LB films transferred during the first compression cycle since the fwhm and the band positions of the polarized, s and p, and unpolarized spectra under normal incidence were different. In contrast, those parameters remain almost unchanged (data shown in Table 2; deviation $\pm 1 \text{ cm}^{-1}$) in the LB film transferred at 35 mN/m during the second successive compression process excepting the fwhm values at 2867 cm^{-1} for the polarized, s and p, spectra (44 and 39 cm^{-1} , respectively). Thus, the $\nu_{\text{as}}(\text{CH}_2)_{\text{cry}}$ and $\nu_s(\text{CH}_2)_{\text{cry}}$ stretches give $D \approx 2.4$, confirming the crystalline state of the alkyl chains with an orientation normal to the substrate. Also, $D \approx 1.4$ has been calculated for the $\nu_{\text{as}}(\text{CH}_3)$ mode corresponding to a random orientation of this group. The D values obtained for the rest of the Gaussian peaks (see Table 2) should be considered with caution because of the possible overlapping of the CH_2 and CH_3 modes or of the CH_2 mode coming from different chemical situations, for example, a small value of D (1.44) was obtained for the $\nu_{\text{as}}(\text{CH}_2)_{\text{liq}}$ stretch (2928 cm^{-1}) that should have a contribution from CH_2 groups of the alkyl chain in the liquid state and from the methylene bridges.

In summary, (i) during the second compression cycle the calix[8]arene molecules organize into a more ordered structure than that in the first cycle and (ii) the alkyl chains adopt a crystalline state in a section of the molecule (lower rim), while the tert-butyl groups in the opposite segment of the molecule (upper rim) show a random orientation (noncrystalline). This phenomenon could be responsible for the absence of a solid phase obtained in the air–water isotherm.

C=O Stretching Region. The band of carboxylic acid groups ($\nu(\text{C}=\text{O})$ mode) has two contributions at least: a shoulder at 1739 cm^{-1} assigned to the unhydrated $\text{C}=\text{O}$ group and a peak at 1708 cm^{-1} corresponding to $\text{C}=\text{O}$ hydrogen-bonded groups.^{49,50} The fit of this band to Gaussian functions allows us to obtain an area close to 70% for all analyzed films. However, this value does not allow us to determine the proportion of the CO group hydrogen bonded without the molar absorptivity of each group.

It is notorious that for the cast film in the absence of water the proportion of CO with hydrogen bonds is similar to that found for the hydrated LB films. This fact should be related to the formation of intermolecular and intramolecular hydrogen bonds in this inhomogeneous film. In the LB film, especially when the alkyl chains are forced to adopt a perpendicular orientation as a result of compression, those hydrogen bonds

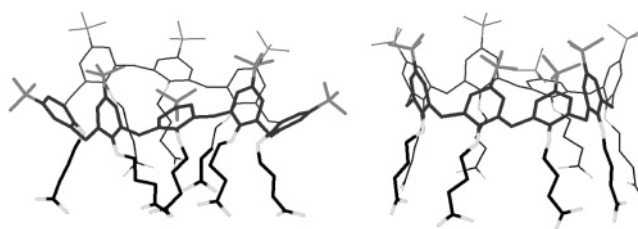


Figure 9. Optimal structures obtained by molecular mechanics simulation. The applied method is described in the Experimental Section.

are broken and replaced with hydrogen bonds with water molecules. We think that this phenomenon leads to the morphological changes observed by BAM during the first and second compression cycles.

A small fraction of dissociated acid groups ($\nu_a(\text{COO}^-)$ mode at 1548 cm^{-1}) is detected for all analyzed LB films. However, that fraction is always larger at 25 than at 35 mN/m for the same cycle.

Discussion and Conclusions

The behavior of the C8A molecules at the air–water interface shows particular features because of their special structure. Thus, it is observed that the properties of the film, for example, isotherms, domain formation, and FTIR spectra, recorded during the first compression cycle differ appreciably from those during the second compression and following cycles.

One of the more noticeable phenomena is the reduction of the molecular area at high surface pressure during the first compression cycle with respect to ensuing compressions. This phenomenon can be interpreted on the basis of the particular conformation with inter- and intramolecular hydrogen bonds of the C8A molecules when they are spread at the interface.

The optimal structure obtained by molecular mechanics simulation according to the method described in the Experimental Section is shown in Figure 9 (left). In this structure, the rim of the calixarene arranges in an irregular egglike form where the tert-butyl groups from different planes are alternatively located inside and outside of the rim. On the other hand, the arrangement of the alkyl chains with their acid groups is not uniform since some of them are directed to the cavity inside while others point outward.

Two intramolecular hydrogen bonds can be detected, and taking into account the arrangement of the acid groups, formation of intermolecular hydrogen bonds between adjacent molecules is expected.

Although the comparison between this model (Figure 9, left) and the cast films has some restrictions, for example, the optimized structure has been obtained under vacuum conditions, the optimized conformer seems to explain the high formation of hydrogen bonds detected in the cast films by FTIR.

The large bright domains observed after spreading the C8A at the air–water interface even at $A \approx 900 \text{ \AA}^2/\text{molecule}$ are indicative of the intramolecular forces that avoid the formation of the gas phase. This phenomenon could be due to the partially conserved structure including intra- and intermolecular hydrogen bonds of the C8A molecule before spreading, which restricts in part the access of the water molecules to the hydrophilic region of the C8A molecule. Therefore, the intermolecular hydrogen bonds would be responsible for the bright domain formation at zero surface pressure.

When the C8A monolayer is compressed for the first time and approaches $A \approx 330 \text{ \AA}^2/\text{molecule}$, the elasticity or compressibility modulus, C_s^{-1} , starts to rise (see Figure 2, bottom)

and a maximum is obtained at π (C_s^{-1}) = 16 mN/m and $A(C_s^{-1})$ = 261 Å²/molecule. Under further compression, C_s^{-1} decreases to an approximately constant nonzero value. Finally, collapse is observed at $A < 200$ Å²/molecule when the compressibility modulus sharply drops to zero. The behavior of the compressibility modulus in the $260 \text{ Å}^2 < A < 200 \text{ Å}^2$ region is unusual. A phase transition cannot explain such a behavior since C_s^{-1} should increase by means of the formation of a more condensed phase. A possible explanation could be as follows: when the monolayer is compressed, the alkyl chains are obliged to stand perpendicularly with respect to the air–water interface, although the presence of hydrogen bonds is opposed to it. At high surface pressure, the intra- and intermolecular hydrogen bonds can break up and new ones with water molecules are formed. The breaking of the intermolecular hydrogen bonds causes the film to offer less opposition to be compressed, and thus a decrease in C_s^{-1} is observed.

At $\pi = 16$ mN/m, where the C_s^{-1} is maximum, the excess of the Gibbs energy with respect to that at $\pi = 0$ mN/m (where the bright domains are already formed) can be determined according to

$$\Delta G = \pi_{C_s^{-1}} \cdot A_{C_s^{-1}} \quad (3)$$

resulting in $\Delta G \approx 6$ kcal·mol⁻¹, which approximately corresponds to the energy needed for hydrogen-bond formation. This calculation is not rigorous because other possible components of the Gibbs energy are ignored. However, qualitatively we can think that the threshold of the minimum energy needed for the breaking of hydrogen bonds in the film is gained at $\pi(C_s^{-1})$ and $A(C_s^{-1})$.

On the other hand, during the first compression the perpendicular orientation of the alkyl chains does not lead to a whole crystalline state, as deduced from the FTIR spectra (Figure 5A, dotted line). The initial arrangement in the bright domains must reduce the free movement of molecules, avoiding such a crystalline order. Also, the tert-butyl groups determining the surface area per molecule can be located at different planes with respect to the interface, and thus a decrease of the molecular area at the same surface pressure with respect to the subsequent compression processes may be measured. This fact could explain the reduction of the area per C8A molecule in the first compression cycle with respect to the second cycle at high surface pressure (see Figure 2, top).

During the expansion, the molecules return to a relaxed conformation where hydrogen bonds with the water molecules are conserved. The properties of the film have changed with respect to the initial spread situation. Thus, the new domains observed are formed by means of van der Waals interactions between molecules, and the energy coming from the laser radiation or from the vibrating plate is sufficient to break up such domains, thus increasing the proportion of gas phase (as observed by BAM, Figure 4).

A following compression leads to the crystalline state of the alkyl chains (FTIR spectra of the LB film transferred at 35 mN/m during the second compression cycle: Figure 5A, solid line) and consequently to a more homogeneous conformation of the molecules in the film. That crystalline order for the alkyl chains must be associated with a rigid structure of the calixarene rim, causing an accessible central cavity, as depicted in Figure 9 (right). Thus, the film is more rigid and the area per molecule is slightly higher than that measured during the first compression cycle at high surface pressure.

The conformation of C8A molecules at the air–water interface must be related to the possible interactions of their

hydrophilic groups. Thus, the presence of intra- and intermolecular hydrogen bonds leads to an inaccessible core by means of the distortion of the central cavity. However, the formation of hydrogen bonds with water molecules induced by the surface pressure may open such a distorted cavity, increasing access to not only the hydrophilic groups but also to the cavity inside.

The great variety of substituents used in calixarene chemistry introduces a complex mixture of inter- and intramolecular forces, which ultimately determines the conformational distribution. This is clearly involved in the success of these types of molecules in applications as diverse as catalysis, enzyme mimics, host–guest chemistry, selective ion transport, and sensors. Therefore, control of the conformation of the calixarene rim, that is, its shape and accessibility, by means of surface pressure can enhance, together with other strategies (modification of substituents both on the upper and lower rim, or of unit number), the range of possible applications of these type of molecules.

Acknowledgment. The authors thank the Spanish CICYT for financial support of this research in the framework of Project BQU2001-1792. Also, we thank the Ministerio de Ciencia y Tecnología for the contract of one of the authors (Ramón y Cajal Program).

References and Notes

- (1) Gutsche, C. D. *Calixarenes*; The Royal Society of Chemistry: Cambridge, MA, 1989.
- (2) *Calixarenes 2001*; Kluwer Academic Publishers: Dordrecht, The Netherlands, 2001.
- (3) Dei, L.; Casnati, A.; Lo Nostro, P.; Baglioni, P. *Langmuir* **1995**, *11*, 1268.
- (4) Dei, L.; Lo Nostro, P.; Capuzzi, G.; Baglioni, P. *Langmuir* **1998**, *14*, 4143.
- (5) Richardson, T.; Greenwood, M. G.; Davis, F.; Stirling, C. J. M. *Langmuir* **1995**, *11*, 4623.
- (6) Davis, F.; O'Toole, L.; Short, R.; Stirling, C. J. M. *Langmuir* **1996**, *12*, 1892.
- (7) Nabok, A. V.; Richardson, T.; Davis, F.; Stirling, C. J. M. *Langmuir* **1997**, *13*, 3198.
- (8) Moreira, W. C.; Dutton, P. J.; Aroca, R. *Langmuir* **1995**, *11*, 3137.
- (9) Castillo, R.; Ramos, S.; Cruz, R.; Martinez, M.; Lara, F.; Ruiz-Garcia, J. *J. Phys. Chem.* **1996**, *100*, 709.
- (10) He, W.; Vollhardt, D.; Rudert, R.; Zhu, L.; Li, J. *Langmuir* **2003**, *19*, 385.
- (11) Van der Heyden, A.; Regnouf-de-Vains, J.-B.; Warszynski, P.; Dalbavie, J.-O.; Zywockinski, A.; Rogalska, E. *Langmuir* **2002**, *18*, 8854.
- (12) Zhang, L.; Zhang, Y.; Tao, H.; Sun, X.; Guo, Z.; Zhu, L. *Thin Solid Films* **2002**, *413*, 224.
- (13) van Hoorn, W. P.; Morshuis, M. G. H.; van Veggel, F. C. J. M.; Reinhoudt, D. N. *J. Phys. Chem. A* **1998**, *102*, 1130.
- (14) Davis, F.; Lucke, A. J.; Smith, K. A.; Stirling, C. J. M. *Langmuir* **1998**, *14*, 4180.
- (15) McCartney, C. M.; Richardson, T. H.; Pavier, M. A.; Davis, F.; Stirling, C. J. M. *Thin Solid Films* **1998**, *329*, 431.
- (16) Fromherz, P. *Rev. Sci. Instrum.* **1975**, *46*, 1380.
- (17) *Hyperchem*, 6th ed.; Hypercube, Inc.: Gainesville, FL, 1999.
- (18) Kane, P.; Fayne, D.; Diamond, D.; Bell, S. E. J.; McKerver, M. A. *J. Mol. Model.* **1998**, *4*, 259.
- (19) Brook, R. A.; Dooling, C. M.; Jones, L. T.; Richardson, T. H. *Mater. Sci. Eng., C* **2002**, *22*, 427.
- (20) Gaines, G. L. J. *Insoluble Monolayers at Liquid–Gas Interfaces*; Wiley-Interscience: New York, 1966.
- (21) Byrd, H.; Whipps, S.; Pike, J. K.; Ma, J.; Nagler, S. E.; Talham, D. R. *J. Am. Chem. Soc.* **1994**, *116*, 295.
- (22) Porter, M. D.; Bright, T. B.; Allara, D. L.; Chidsey, C. E. D. *J. Am. Chem. Soc.* **1987**, *109*, 3559.
- (23) Tao, Y. T. *J. Am. Chem. Soc.* **1993**, *115*, 4350.
- (24) Tang, X. Y.; Schneider, T.; Buttry, D. A. *Langmuir* **1994**, *10*, 2235.
- (25) Neumann, V.; Gericke, A.; Hühnerfuss, H. *Langmuir* **1995**, *11*, 2206.
- (26) Hühnerfuss, H.; Gericke, A.; Neumann, V.; Stine, K. J. *Thin Solid Films* **1996**, *285*, 694.
- (27) Moreira, W. C.; Dutton, P. J.; Aroca, R. *Langmuir* **1994**, *10*, 4148.

- (28) Du, X.; Shi, B.; Liang, Y. *Langmuir* **1998**, *14*, 3631.
- (29) Oliviere, P.; Yarwood, J.; Richardson, T. H. *Langmuir* **2003**, *19*, 63.
- (30) Tillman, N.; Ulman, A.; Schildkraut, J. S.; Penner, T. L. *J. Am. Chem. Soc.* **1988**, *110*, 6136.
- (31) In *FTIR in Colloid and Interface Science*; Scheuing, D. R., Ed.; American Chemical Society: Washington, D.C., 1991; Vol. 447.
- (32) Ulman, A. *An Introduction to Ultrathin Organic Films from Langmuir-Blodgett to Self Assembly*; Academic Press: San Diego, CA, 1991.
- (33) Taniike, K.; Matsumoto, T.; Sato, T.; Ozaki, Y.; Nakashima, K.; Iriyama, K. *J. Phys. Chem.* **1996**, *100*, 15508.
- (34) Yong, H.; Penner, T. L.; Whitten, D. G. *Langmuir* **1994**, *10*, 2757.
- (35) Rabolt, J. F.; Burns, F. C.; Schlatter, N. E.; Swalen, J. D. *J. Chem. Phys.* **1983**, *78*, 946.
- (36) Zhao, B.; Li, H.; Zhang, X.; Shen, J.; Ozaki, Y. *J. Phys. Chem. B* **1998**, *102*, 6515.
- (37) Katayama, N.; Enomoto, S.; Sato, T.; Ozaki, Y.; Kuramoto, N. *J. Phys. Chem.* **1993**, *97*, 6880.
- (38) Snyder, R. G.; Strauss, H. L.; Elliger, C. A. *J. Phys. Chem.* **1982**, *86*, 5145.
- (39) Snyder, R. G.; Maroncelli, M.; Strauss, H. L.; Hallmark, V. M. *J. Phys. Chem.* **1986**, *90*, 5623.
- (40) Bellamy, L. J. *The Infra-red Spectra of Complex Molecules*, 2nd ed.; John Wiley & Sons: New York, 1964.
- (41) Laibinis, P. E.; Whitesides, G. M.; Allara, D. L.; Tao, Y. T.; Parikh, A. N.; Nuzzo, R. G. *J. Am. Chem. Soc.* **1991**, *113*, 7152.
- (42) Nuzzo, R. G.; Dubois, L. H.; Allara, D. L. *J. Am. Chem. Soc.* **1990**, *112*, 558.
- (43) Nuzzo, R. G.; Fusco, F. A.; Allara, D. L. *J. Am. Chem. Soc.* **1987**, *109*, 2358.
- (44) Urban, M. W. *Vibrational Spectroscopy of Molecules and Macromolecules on Surfaces*; John Wiley & Sons: New York, 1993.
- (45) Stannersa, C. D.; Dua, Q.; China, R. P.; Cremerb, P.; Somorjaib, G. A.; Shen, Y.-R. *Chem. Phys. Lett.* **1995**, *232*, 407.
- (46) Sinniah, K.; Cheng, J.; Terrettaz, S.; Reutt-Robey, J. E.; Miller, C. J. *J. Phys. Chem.* **1995**, *99*, 14500.
- (47) Gao, W.; Dickinson, L.; Grozinger, C.; Morin, F. G.; Reven, L. *Langmuir* **1996**, *12*, 6429.
- (48) Vandevyver, M.; Barraud, A.; Ruaudel-Teixier, A.; Maillard, P.; Gianotti, C. J. *Colloid Interface Sci.* **1982**, *85*, 571.
- (49) Gericke, A.; Hühnerfuss, H. *J. Phys. Chem.* **1993**, *97*, 12899.
- (50) Gericke, A.; Hühnerfuss, H. *Langmuir* **1995**, *11*, 225.